J Solid State Electrochem (2018) 22:1557–1562
DOI 10.1007/s10008-017-3768-z

ORIGINAL PAPER

Electrodeposition of Fe-doped Sb_2Se_3 thin films for photoelectrochemical applications and study of the doping effects on their properties

Magno Barcelos Costa[1] · **Francisco Willian de Souza Lucas**[1] · **Lucia Helena Mascaro**[1]

Received: 13 July 2017 / Revised: 4 September 2017 / Accepted: 5 September 2017 / Published online: 20 September 2017

Abstract Sb_2Se_3 (SSe) has been highlight as a low-cost, less complex, low toxicity, and earth-abundant photovoltaic (PV) absorber not only because of its excellent properties but also because of its demonstrated 5.6% certified efficiency and decent device stability. An understanding of the effects of intentional dopants on the properties of this material would help to further improve SSe PV devices. In this work, Fe-doped SSe thin film was obtained by electrodeposition at different levels of doping, which is an easy, cheap, and scalable technique. At the studied levels, this dopant caused low influence in band gap and morphologic-structural properties of the films; however, it did impact their electronic properties and photoactivity toward hydrogen gas evolution. The film obtained from a deposition bath composed of 5% of Fe presented a photocurrent similar to that shown by the undoped film, despite showing a carrier density that was three orders of magnitude higher. This behavior makes us believe that, compared to the undoped film, a photovoltaic device made with this 5% Fe-doped film would have a higher fill factor and efficiency.

Keywords Antimony selenide · Photoelectrochemistry · Water splitting · Less complex, low toxicity, and earth-abundant semiconductor · One-dimensional $(Sb_4Se_6)_n$ ribbons

✉ Francisco Willian de Souza Lucas
willlucas@yahoo.com.br

✉ Lucia Helena Mascaro
lmascaro@ufscar.br

[1] Interdisciplinary Laboratory of Electrochemistry and Ceramics (LIEC), Federal University of São Carlos, Road Washington Luiz, km 235, São Carlos, SP 13565-905, Brazil

Introduction

Recently, the use of thin films of antimony selenide (SSe) as an absorber for photovoltaic (PV) devices has attracted the attention of researchers [1, 2]. This increasing interest is due to the fact that SSe is composed of more abundant components and presents lower toxicity, structural complexity, and melting point (grain growth at lower temperature) compared to the more representative films in the market, such as CdTe, Cu(In,Ga)Se (CIGS), and Cu(Zn,Sn)Se (CZTSe) [3]. In addition, SSe has a direct and indirect optical band gap within a range of 1.00 and 1.13 eV, which makes it an adequate absorber material for single-junction solar cells [4–7].

To reduce costs, researchers have not only looked for cheaper and earth-abundant materials but also for a more economically viable fabrication process for these materials. In this line of reasoning, the electrodeposition has been widely used in several works; this is because it is an easy, cheap, and scalable technique with good reproducibility, and it maintains electrodeposits with the desired quality [8–13].

In addition to the search for new material and methods, different approaches have been used to improve the photovoltaic-interesting properties of the more representative and known materials, such as annealing [13, 14], chemical treatment [15, 16], and doping [17, 18]. In the case of doping, several effects are expected, such as modulation of the band gap [19, 20], increase of the grain size [17], passivation of defects [18, 21], increase in film conductivity (an increase of carrier concentration, and a decrease of the series resistance of the solar cell [6, 7]) [22], and improvement in photoactivity [18–21], among other beneficial or harmful effects. Thus, the study of the influence of dopants on the SSe properties becomes an important factor for its applications. It is noteworthy that the literature is scarce regarding doped SSe thin films by means of electrodeposition, and it is even scarcer concerning

the effects of dopants on photoelectrochemical activity. Li and co-authors electrodeposited and characterized Bi-alloy SSe thin films, obtaining a high content of bismuth incorporation (> 10 at%) [23] and observing an *n*-type conductivity. In 2016, Li and co-authors doped SSe thin films obtained via the hydrazine solution process with 0.1% of Fe and Mg. Their results showed that Mg-doping was inert to the electric properties of the SSe, while Fe introduced harmful *n*-type doping [24]. The carrier concentrations of the films did not change with doping and remained as low (~ 10^{13} cm^{-3}) as the undoped ones, which could be evidence of no true incorporation of the dopant into the SSe crystal. However, in both studies, the effects of this doping on the photoelectrochemical activity of the SSe were not evaluated.

Based on the aforementioned background, the present work reports the electrodeposition of Fe-doped SSe thin films, with different dopant concentrations. It also describes the study of the doping effects on the morphological, structural, optoelectronic, and photocatalytic properties of this material. Iron was chosen as a dopant because it is a catalyst in the hydrogen release process commonly used in water splitting [25], as well as being an earth-abundant element.

Method

The following reagents used during this work were of an analytical grade: Na_2SO_4 (Sigma-Aldrich, > 99.9%), H_2SO_4 (Sigma-Aldrich, 98%), $K(SbO)C_4H_4O_6 \cdot 0.5\ H_2O$ (Sigma-Aldrich, > 99%), SeO_2 (Alfa Aesar, > 99,4%), Se powder (Vetec, ≥ 99%), and e $FeSO_4 \cdot 7\ H_2O$ (Sigma-Aldrich, ≥ 99%). All electrochemical measurements were performed on a Metrohm-Eco Chemie potentiostat/galvanostat (Autolab PGSTAT302N) using a conventional cell with three-electrode system. For the working electrode, fluorine-doped tin oxide (FTO, 7 Ω/sq., MTI Corporation) coated glass was used, while Pt plate was used as the auxiliary electrode. $Ag/AgCl/Cl^-_{(sat\ KCl)}$ was used as a reference electrode, and all potentials in the present work are related to this reference. FTO was cut into small pieces (1.5 cm × 1.0 cm) and subsequently ultrasonized with deionized water, ethanol, acetone, and isopropanol for 5 min in each solvent. After that, the FTO substrates were immersed in a solution of 0.5 mol L^{-1} $KMnO_4$ for 1 h and then alternately washed with 30% H_2O_2 and deionized water. Hydrophilization of the FTO electrodes was done at 70 °C for 1 h in a solution of H_2O/H_2O_2 (conc.)/NH_4OH (conc.), in a proportion of 5:1:1, respectively. At last, it was rinsed with deionized water and dried in an $N_{2(g)}$ stream (Linde, 99.9%).

The SSe films were obtained by co-electrodeposition (approximately 1 cm^2 of area) under potentiostatic conditions. The deposition bath consisted of solutions of 2.0 mmol L^{-1} SeO_2 and 2.5 mmol L^{-1} $K(SbO)C_4H_4O_6$ with $FeSO_4$ 0.125, 0.5, and 1.25 mmol L^{-1}, i.e., 5, 20, or 50% of the dopant (relative to the Sb content in the bath). For the supporting electrolyte, a solution of 0.5 mol L^{-1} Na_2SO_4 was used, with a pH adjusted to 2 by the addition of drops of concentrated H_2SO_4. The bath solution was previously deaerated with a stream of $N_{2(g)}$ introduced into each solution during 3 min before deposition. From the previously optimized conditions [26], the electrodeposition was performed until it reached 600 mC of total charge (to maintain the film thickness between 300 and 400 nm, which is usually used in the literature [4, 27]), applying a potential of −0.6 V, followed by thermal treatment at 300 °C for 3 h. It is important to mention that, in general, the low crystallinity of the films obtained by electrodeposition is a limitation of this method. This makes it necessary to use a subsequent thermal treatment, already studied in detail by our group [26]. Thus, the thermal treatment was carried out in a tubular furnace at a heating rate of 10 °C min^{-1} and with the N_2 atmosphere maintained at 1 atm. The heated gas was brought to a bubbler filled with mineral oil under a flow of 1 mL min^{-1}. Inside the tube furnace, a lead borosilicate glass cylinder of approximately 300 mL was placed. In the latter, the films were placed between two crucibles containing, in each, 0.2 g of selenium powder to maintain a controlled Se-rich atmosphere.

The physical characterization of the films was made initially from their morphology and structural data, measured, respectively, by high-resolution field-emission scanning electron microscopy (FE-SEM, Zeiss Supra 35) and by Rigaku X-ray diffractometer (DMax2500PC) with CuKα radiation, with a counting time of 6 s and a scanning step of 0.02 °. Their composition was measured by energy dispersive X-ray (EDX) spectroscopy (FEI-XL30-FEG with an Oxford Instruments-Link ISIS 300 detector), while the determination of their band-gap energies was performed by an NIR-UV-vis spectrometer with diffuse reflectance geometry (Cary 5E spectrometer) from 800 to 1800 nm. The band-gap energy (E_g) was estimated using the following equations: [11, 28, 29]

$$\alpha = F(R) = \frac{(1-R)^n}{2R} \quad and \quad (\alpha h\nu)^n = A\left(h\nu - E_g\right) \tag{1}$$

where $F(R)$ is the Kubelka-Munk function, R is the absolute reflectance to a given value of $h\nu$, α is the absorption coefficient, h is the Planck constant, ν is the frequency, and n assumes the values of 2 or 2/3 for direct transition (allowed and forbidden, respectively) and 1/2 or 1/3 for indirect (allowed and forbidden, respectively).

The flat band potential (E_{fb}) (and consecutive, band position), the charge carrier density (N_D), and the semiconductor type (*n- or p-*) were determined by the Mott-Schottky. The Mott-Schottky experiments were performed using the same supporting electrolyte used in the electrodeposition and were

carried out by means of potentiodynamic electrochemical impedance spectroscopy, applying a 0.01 V_{rms} sinusoidal excitation signal with a frequency of 1, 5, and 10 kHz. The results were described by the following equation for *p*-type semiconductors: [30–32]

$$C_{sc}^{-2} = -2(eN_A\varepsilon_0\varepsilon_{sc})^{-1}\left[E - E_{fb} + \left(k_BTe^{-1}\right)\right] \quad (2)$$

where C_{sc} is the semiconductor capacitance of the space charge region, e is the elementary charge, N_A is the charge carrier density (or acceptors density for p-type semiconductors), ε_0 the permittivity of free space, ε_{sc} is the semiconductor dielectric constant, E is the applied potential, E_{fb} is the flat band potential, k_B is the Boltzmann constant, and T is the absolute temperature. Using the Mott-Schottky graph, the N_A can be calculated from the slope, and the E_{fb} can be obtained from the extrapolation to $C_{sc}^{-2} = 0$.

The photoelectrochemical characterization was performed with a solar simulator with a 150 W xenon lamp (Newport 66902) and an AM 1.0 lens as the light source, using a quartz window electrochemical cell with 1 cm optical path between the window and the surface of the films.

Results and discussions

Physical characterization

First, to study the doping effect on the morphological properties of the SSe films, their surface images were obtained by FE-SEM, which can be seen in Fig. 1.

The films showed good adhesion to the substrate, with thicknesses of ~ 400 nm (seen in cross-section micrographs). In general, it was visually observed that these surfaces did not present significant differences in their morphology in term of their doping concentration, being rough, homogeneous, and presenting forms not well defined in all conditions. However, it is possible to observe a slight tendency to the formation of nano-rods in Fig. 1b, which represents the film Fe-doped from a bath with 5% of dopant.

Thus, in sequence, the composition, crystalline structure, and band gap of the films were characterized, and the data is organized in Table 1. The diffractograms and the graph of $(\alpha h\nu)^2$ vs. photon energy can be checked in Figs. 2 and 3, respectively.

As can be seen in Table 1, the EDS analyses showed that the composition of Fe-doped films is close to the stoichiometric, as indicated in the non-doped film. The incorporation of Fe into the SSe films was low compared to its concentration in the deposition bath. This can be explained by the fact that the Fe deposition potential be more negative than those for Sb and Se [33].

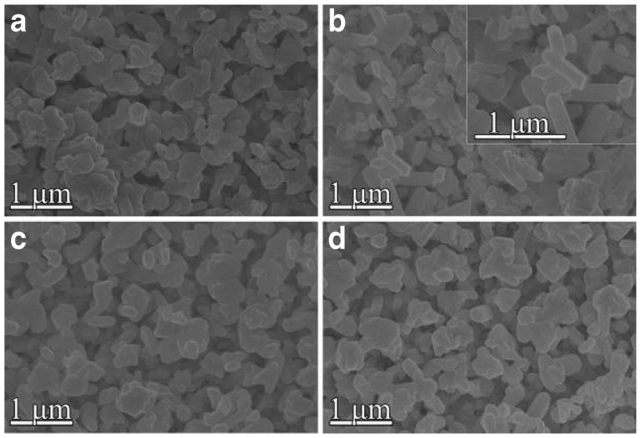

Fig. 1 Surface FE-SEM micrographs of SSe thin films with 50kx of magnification. **a** Non-doped film and those obtained from electrolytic bath with **b** 5%, **c** 20%, and **d** 50% of Fe ions (relative to Sb content in the bath)

In Fig. 2a, we can see that the Fe-doped films presented all the characteristic peaks of the orthorhombic Sb_2Se_3 pattern, except for the presence of a secondary Sb_2O_3 cubic phase (Senarmontite, syn JCPDF 71–365) for the 50% Fe-doped film, which could be inferred by the peak at $2\theta = 27.7°$ with very low intensity. The crystallographic parameters extracted from the X-ray diffraction patterns (Table 1) show that the incorporation of Fe into SSe did not change its cell unit significantly. This behavior was expected once the ionic radii of the Fe and of the Sb was similar [34] and the incorporated Fe content was low. In addition to the previous characterisations, Fig. 2b (also Table 1) shows that this small incorporation of Fe did not decrease the band gap of the films (expected for high Fe-doping), which is a good result, since the SSe already has an appropriate band gap to be used in a single-junction solar cell [5, 7]. It is also good to mention that these optical band gap values agree with those found in the literature [9, 35, 36].

Summarizing the physical characterizations, the low incorporation of Fe ions into the SSe thin film did not change noticeably its morphology, composition, structure (except by the presence of a small quantity of Sb_2O_3 impurity on the 50% Fe-doped film), and band gap. Thus, it is worth analyzing the effect of this dopant on the electronic and photoactivity properties of this material.

Electrochemical and photoelectrochemical characterization

At last, in order to observe whether these small Fe-doping levels affect the electronics and photoactivity of the SSe films, experiments of Mott-Schottky (M-S) and the transients of the photocurrent were performed. Figure 3a and b show the M-S and photocurrent graphs for the undoped and doped films. For better visualization of the results, the values of flat band potential (E_{fb}) and acceptors density (N_A) (extracted from

Table 1 Composition, unit-cell parameters, and optical band gap for the electrodeposited SSe films

SSe films	Composition %atm*			Unit-cell parameters				E_g / eV
	Sb	Se	Fe	*a* / Å	*b* / Å	*c* / Å	*V* / Å^3	
Non-doped film	39.2	60.8	n.d.	11.57	11.74	3.97	539.13	1.09
Fe 5%	36.8	62.4	0.8	11.55	11.78	3.99	543.74	1.07
Fe 20%	39.6	59.2	1.2	11.57	11.78	3.98	542.80	1.09
Fe 50%	39.6	58.9	1.5	11.57	11.71	3.97	538.12	1.09
JCPDF 89–821	–	–	–	11.59	11.74	3.95	538.23	–

*The standard deviation was lower than 5%, with 95% confidence.

n.d non-detected

Fig. 3a) and the photocurrents (extracted from Fig. 3b) are organized in Table 2.

From the M-S angular coefficient seen in Fig. 3a, we can conclude that all the films are *p*-type semiconductors, independent of the doping level. Taking into account that the E_{fb} for the *p*-type semiconductors is close to the valence band maximum (VBM) [5–7], these values perfectly agree with those obtained by Xinsheng Liu and co-authors [37]. They determined the VBM of thermo-evaporated SSe films by

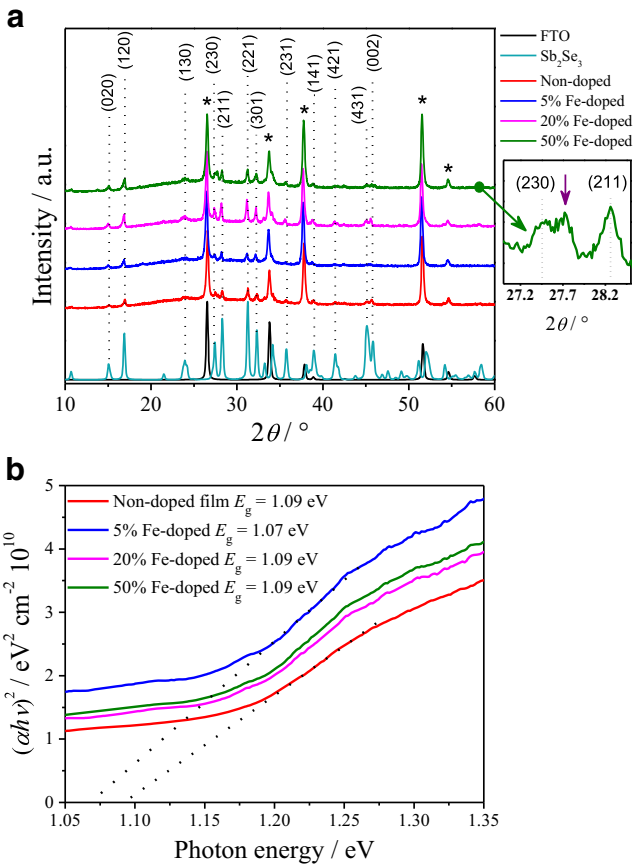

Fig. 2 **a** X-ray diffraction patterns of the SSe films submitted to different Fe-doping conditions. The standard SnO_2 (representing FTO, JCPDF 77–451) and Sb_2Se_3 (JCPDF 89–821) diffraction patterns are shown in the lower region of the graph for comparison. For the 50% Fe-doped film, a zoom of the region of 2θ between 27 and 28.5° is shown, highlighting the extra peak associated with impurities. **b** The plot of $(\alpha h\nu)^2$ vs. photon energy. The value of the linear extrapolation at the *x*-axis is equal to the band gap (E_g)

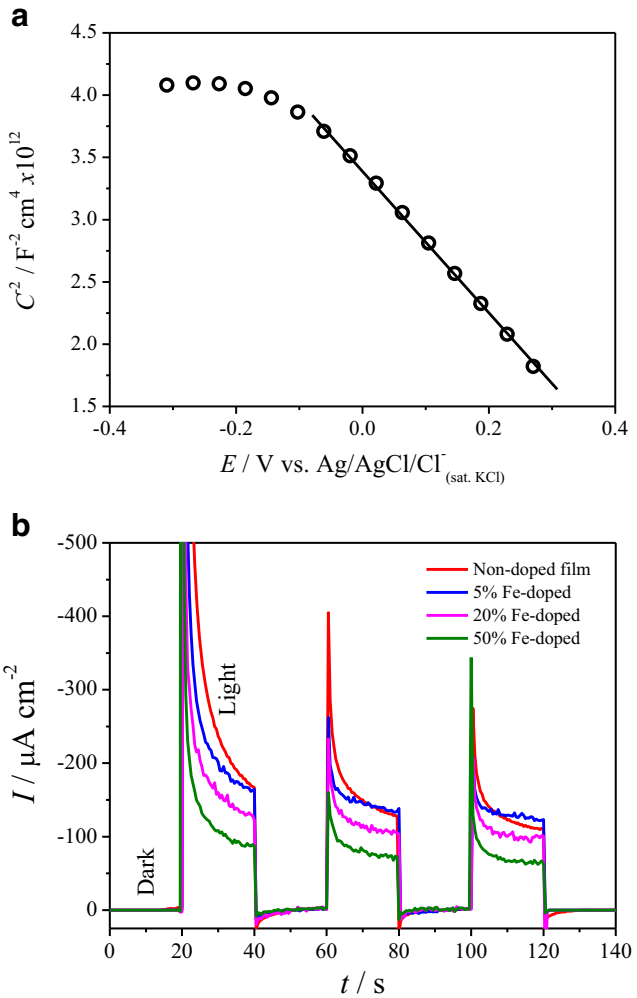

Fig. 3 **a** Mott-Schottky graph for the 50% Fe-doped SSe film performed in 0.5 mol L^{-1} Na_2SO_4/H_2SO_4– pH 2 by applying a sinusoidal excitation of 0.01 V_{rms} with the frequency of 5 kHz. **b** Photocurrent transient at the standard hydrogen reduction potential, −0.315 V vs. Ag/AgCl/$Cl^-_{(sat. KCl)}$, for the undoped and Fe-doped SSe films. The light intensity incident on the electrode was adjusted to 100 mW cm^{-2} and the solar spectrum was simulated with an AM 1.0 lens

Table 2 Photocurrent intensity and carrier density for electrodeposited non-doped and doped SSe films

SSe films	Current density* / μA cm^{-2}	Flat band potential** / eV vs. vacuum	Carries density / cm^{-3}
Non-doped film	166.34	−5.27	3.7×10^{16}
Fe 5%	165.13	−5.23	1.0×10^{19}
Fe 20%	121.18	−5.23	3.2×10^{17}
Fe 50%	87.54	−5.23	3.5×10^{18}
Non-doped film ref. [37]	–	−5.35	1.1×10^{15}

*At standard hydrogen reduction potential in 0.5 M Na_2SO_4/H_2SO_4 at pH 2, −0.315 V vs. $Ag/AgCl/Cl^-_{(sat.\ KCl)}$. Standard deviation ($n$ = 3) was lower than 8%, with 95% confidence.

**[E vs. vacuum] = [E vs. $Ag/AgCl/Cl^-_{(sat.\ KCl)}$] − 4.24 eV [38]

ultraviolet photoelectron spectroscopy (UPS) measurements [37]. Observing the N_A in Table 2, we can see that the films obtained from a deposition bath composed of 5% Fe showed higher acceptor density (three orders higher than the undoped film), i.e., it had a lower resistivity [5–7]. The carrier density decreased for the 20% Fe-doped film and increased for the 50% Fe-doped one. The decrease in N_A could be explained by the introduction of donor defects when the Fe content in the film was increased. These defects could partially compensate the acceptor defects that are responsible by the SSe p-type conductivity, a phenomenon already observed by Li and co-authors [24]. In turn, the fact that the N_A for the 50% Fe-doped film was higher than the 20% Fe-doped film could be associated with the impurity phase of the Sb_2O_3, present in the film.

At last, in Fig. 3b, it is possible to observe a cathodic photocurrent of the $H_{2(g)}$ evolution for all the films, which is an indication of p-type conductivity, thereby agreeing with the behavior observed from the M-S graph. Based on the values of the photocurrent (Table 2), it is possible to observe that the 5% Fe-doped film presented a photocurrent that was very close to that shown by the undoped film. This is a very interesting behavior, as the Fe-doping at this level promoted an increase of the carrier's density by three orders of magnitude without affecting its already good photocurrent. At this doping level, this phenomenon may be evidence that Fe ions have increased the shallow acceptor defects density. Whereas, in the 20 and 50% Fe-doped films, may have occurred the insertion of deep donor defects, recombination centers, which justify the reduction of photocurrent, similar to the one observed by Li and co-authors for a PV device [24]. Beyond this, for 50% Fe-doped film, the decrease in photoactivity could also be associated with the presence of Sb_2O_3 impurity. Compared to the undoped film, this film electrodeposited from a bath with 5% of Fe should have lower resistivity, and thus, in consequence, a photovoltaic device made with this film would have a higher fill factor and efficiency, as it would promote a lower series resistance of the device [6, 7].

It is important to emphasize that the photocurrent values (for hydrogen gas evolution) of the present work are approximately three times greater than those seen in the literature for the same material [9]; however, these values are still lower than those observed for more developed hydrogen catalytic materials, such as MoS_2, Ni_2P [39], and Ni-based alloys [40]. This leads us to seek new ways to achieve a competitive and satisfactory efficiency when compared to other materials. An idea for future works would be the deposition of MoS quantum-dots on Sb_2Se_3, as done by Zhang and co-authors on $ZnIn_2S_4$, as well as the fabrication of Pt-decorated/ZnO/CdS/Sb_2Se_3 heterostructures, which proved to be efficient in the production of hydrogen with the use of CIGS as the absorber [41].

Conclusion

It was possible to obtain Fe-doped Sb_2Se_3 (SSe) thin films at different levels of doping by means of an easy, cheap, and scalable technique of electrodeposition. The study of the effects of this dopant into the SSe showed low interference in its band gap and morphologic-structural properties; however, it did greatly impact its electronic properties and photoactivity. The film obtained from a deposition bath composed of 5% Fe presented a photocurrent similar to that shown by the undoped film, despite the fact that it showed a hole density three orders of magnitude higher. This behavior makes us believe that, compared to the undoped film, a photovoltaic device made with this 5% Fe-doped film would have a higher fill factor and efficiency.

Acknowledgments This work was supported by National Counsel of Technological and Scientific Development (CNPq) and the São Paulo Research Foundation (FAPESP), grant #2016/10513-3 and CEPID grant #2013/07296-2.

References

1. Shi X, Zhang X, Tian Y, Shen C, Wang C, Gao H (2012) Electrodeposition of Sb_2Se_3 on indium-doped tin oxides substrate: nucleation and growth. Appl Surf Sci 258:2169–2173
2. Tang A, Long M, He Z (2014) Electrodeposition of Sb_2Se_3 on TiO_2 nanotube arrays for catalytic reduction of p-nitrophenol. Electrochim Acta 146:346–352
3. Zeng K, Xue D-J, Tang J (2016) Antimony selenide thin-film solar cells. Semicond Sci Technol 31:1–13
4. Rodríguez-Lazcano Y, Pena Y, Nair MTS, Nair PK (2005) Polycrystalline thin films of antimony selenide via chemical bath deposition and post deposition treatments. Thin Solid Films 493:77–82
5. Sze SM, Ng KK (2007) Physics of semiconductor devices, 3rd edn. Wiley, New York
6. Grundman M (2010) The physics of semiconductors: an introduction including nanophysics and applications, 3rd edn. Springer, Berlin
7. Yu PY, Cardona M (2010) Fundamentals of semiconductors: physics and materials properties, 3rd edn. Springer, Berlin
8. Tlig F, Gannouni M, Assaker IB, Chtourou R (2017) New investigation on the physical and electrochemical properties of (TAS) thin films grown by electrodeposition technique. J Photochem Photobiol A Chem 335:26–35
9. Lai Y, Chen Z, Han C, Jiang L, Liu F, Li J, Liu Y (2012) Preparation and characterization of Sb_2Se_3 thin films by electrodeposition and annealing treatment. Appl Surf Sci 261:510–514
10. Hossain MA, Al-Gaashani R, Hamoudi H, Al-Marri MJ, Hussein IA, Belaidi A, Merzougui BA, ALharbi FH, Tabet N (2017) Controlled growth of Cu_2O thin films by electrodeposition approach. Mater Sci Semicond Process 63:203–211
11. Lucas FWS, Lima ARF, Mascaro LH (2015) Glycerol as additive in copper indium gallium diselenide electrodeposition: morphological, structural and electronic effects. RSC Adv 5:18295–18300
12. Gromboni MF, Lucas FWS, Mascaro LH (2014) Optical properties and surface morphology of ZnTe thin films prepared by multiple potential steps. J Braz Chem Soc 23:526–531
13. Ullah S, Mollar M, Marí B (2016) Electrodeposition of $CuGaSe_2$ and $CuGaS_2$ thin films for photovoltaic applications. J Solid State Electrochem 20:2251–2257
14. Lucas FWS, Welch AW, Baranowski LL, Dippo PC, Hempel H, Unold T, Eichberger R, Blank B, Rau U, Mascaro LH, Zakutayev A (2016) Effects of thermochemical treatment on $CuSbS_2$ photovoltaic absorber quality and solar cell reproducibility. J Phys Chem C 120:18377–18385
15. Fairbrother A, García-Hemme E, Izquierdo-Roca V, Fontané X, Pulgarín-Agudelo FA, Vigil-Galán O, Pérez-Rodríguez A, Saucedo E (2012) Development of a selective chemical etch to improve the conversion efficiency of Zn-rich Cu_2ZnSnS_4 solar cells. J Am Chem Soc 134:8018–8021
16. Chavda A, Patel M, Mukhopadhyay I, Ray A (2016) Facile, noncyanide based etching of spray deposited Cu_2ZnSnS_4 thin films for secondary phase removal. ACS Sustain Chem Eng 4:2302–2308
17. Yang C, Wang Y, Li S, Wan D, Huang F (2012) $CuSbSe_2$-assisted sintering of $CuInSe_2$ at low temperature. J Mater Sci 47:7085–7089
18. Altamura G, Wang M, Choy K-L (2016) Influence of alkali metals (Na, Li, Rb) on the performance of electrostatic spray-assisted vapor deposited $Cu_2ZnSn(S,Se)_4$ solar cells. Sci Rep 6:22109
19. El Ruby MA, Rohani S (2011) Modified TiO_2 nanotube arrays (TNTAs): progressive strategies towards visible light responsive photoanode, a review. Energy Environ Sci 4:1065
20. Asaduzzaman M, Hasan M, Bahar AN (2016) An investigation into the effects of band gap and doping concentration on $Cu(In,Ga)Se_2$ solar cell efficiency. SpringerPlus 5:578
21. Liu X, Chen C, Wang L, Zhong J, Luo M, Chen J, Xue D-J, Li D, Zhou Y, Tang J (2015) Improving the performance of Sb_2Se_3 thin film solar cells over 4% by controlled addition of oxygen during film deposition. Prog Photovolt Res Appl 23:1828–1836
22. Li D-F, Luo M, Li B-L, Wu C-B, Deng B, Dong H-N (2013) Low-resistivity p-type doping in Wurtzite ZnS using codoping method. Adv Condens Matter Phys 2013:1–4
23. Li J, Wang B, Liu F, Yang J, Li J, Liu J, Jia M, Lai Y, Liu Y (2011) Preparation and characterization of Bi-doped antimony selenide thin films by electrodeposition. Electrochim Acta 56: 8597–8602
24. Li Y, Zhou Y, Zhu Y, Chen C, Luo J, Ma J, Yang B, Wang X, Xia Z, Tang J (2016) Characterization of Mg and Fe doped Sb_2Se_3 thin films for photovoltaic application. Appl Phys Lett 109:1–6
25. Abdi FF, Chemseddine A, Berglund SP, van de Krol R (2016) Assessing the suitability of iron tungstate (Fe_2WO_6) as a photoelectrode material for water oxidation. J Phys Chem C 121: 153–160
26. Costa MB, de Souza Lucas FW, Mascaro LH (2017) Thermal treatment effects on electrodeposited Sb_2Se_3 photovoltaic thin films. ChemElectroChem 4:1–9
27. Ngo TT, Chavhan S, Kosta I, Miguel O, Grande HJ, Tena-Zaera R (2014) Electrodeposition of antimony selenide thin films and application in semiconductor sensitized solar cells. ACS Appl Mater Interfaces 6:2836–2841
28. Nowak M, Kauch B, Szperlich P (2009) Determination of energy band gap of nanocrystalline SbSI using diffuse reflectance spectroscopy. Rev Sci Instrum 80:46107
29. de Lucas FWS, Lima ARF, Mascaro LH (2014) The electrodeposition of Ga-doped $CuInSe_2$ thin film in the presence of Triton 100-X. Electrochim Acta 147:47–53
30. Gelderman K, Lee L, Donne SW (2007) Flat-band potential of a semiconductor: using the Mott–Schottky equation. J Chem Educ 84:685–688
31. Albery WJ, O'Shea GJ, Smith AL (1996) Interpretation and use of Mott-Schottky plots at the semiconductor/electrolyte interface. J Chem Soc Faraday Trans 92:4083–4085
32. Bott AW (1998) Electrochemistry of semiconductors. Curr Sep 17: 87–91
33. Zoski CG (2007) Handbook of electrochemistry, 1st edn. Elsevier, New Mexico
34. Lide DR (2010) CRC handbook of chemistry and physics, 90nd edn. CRC Press, Boca Raton
35. Lai Y, Han C, Lv X, Yang J, Liu F, Li J, Liu Y (2012) Electrodeposition of antimony selenide thin films from aqueous acid solutions. J Electroanal Chem 671:73–79
36. Torane AP, Rajpure KY, Bhosale CH (1999) Preparation and characterization of electrodeposited Sb_2Se_3 thin films. Mater Chem Phys 61:219–222
37. Liu X, Chen J, Luo M, Leng M, Xia Z, Zhou Y, Qin S, Xue D-J, Lv L, Huang H, Niu D, Tang J (2014) Thermal evaporation and characterization of Sb_2Se_3 thin film for substrate Sb_2Se_3/CdS solar cells. ACS Appl Mater Interfaces 6:10687–10695
38. Beranek R (2011) (Photo)electrochemical methods for the determination of the band edge positions of TiO_2-based nanomaterials. Adv Phys Chem 2011:1–20
39. Vesborg PCK, Seger B, Chorkendor I (2015) Recent development in hydrogen evolution reaction catalysts and their practical implementation. J Phys Chem Lett 6:951–957
40. Gong M, Wang DY, Chen CC, Hwang BJ, Dai H (2016) A mini review on nickel-based electrocatalysts for alkaline hydrogen evolution reaction. Nano Res 9:28–46
41. Mali MG, Yoon H, Joshi BN, Park H, Al-Deyab SS, Lim DC, Ahn S, Nervi C, Yoon SS (2015) Enhanced photoelectrochemical solar water splitting using a platinum-decorated CIGS/CdS/ZnO photocathode. ACS Appl Mater Interfaces 7:21619–21625